Original Article

High Performance Polymers

High Performance Polymers
2019, Vol. 31(8) 986–995

DOI: 10.1177/0954008318815733
journals.sagepub.com/home/hip
SAGE

Fabrication of low dielectric constant polyimide/TiO_2 nanofibers with enhanced UV-light shielding properties

Lei Wang[1], Guifen Gong[1], Junyao Shen[2] and Jinsong Leng[2]

Abstract

Polyimide (PI)/titanium dioxide (TiO_2) composite nanofibers (NFs) with average diameters of 200–250 nm were synthesized via electrospinning. The total number density of dipoles decreased significantly, owing to the porous structures and compact interface between TiO_2 NPs and PI matrix. All PI/TiO_2 NFs maintain low dielectric constants and losses. For example, the dielectric constants of PI/TiO_2-6% NFs are all lower than 2.6, being exposed to temperatures from 25°C to 200°C. Meantime, the dielectric losses of PI/TiO_2-6% NFs are below 0.005. For ultraviolet (UV)-light shielding performance, the PI/TiO_2 NFs exhibited good UV-light shielding and corresponding anti-photoaging properties. The reason can be ascribed from high UV-light absorption and scattering ability in the TiO_2 NPs. The best UV-light absorption (average: 3.71) and corresponding absorption decay (15.13%) were achieved for optimized PI/TiO_2-6% NFs. Other fundamental characteristics, such as the thermal stability, mechanical tensile property, and hydrophobicity, were also investigated. Such low dielectric constant PI/TiO_2 composite NFs can be alternatively chosen under a longtime UV-light exposing condition.

Keywords

Polyimide-based composite, dielectric properties, UV-light shielding

Introduction

Pursuing high performance of low-k materials is always a key part for the development of electronics. For example, it has been proved that low-k materials as the core component can reduce interconnect resistive-capacitive (RC) delays, cross-talk noise, and power consumption in the ultra large-scale integrated circuits. Nowadays, exploring polyimide (PI) with high-performance low-k properties has received great enthusiasms due to its high thermal stability, mechanical properties, and chemical inertness.[1–4] PI has been used as interconnect dielectrics for over half a century due to its high thermal stability, mechanical properties, and chemical inertness.[5–7] However, commercialized PI products such as Kapton H, Upilex-S, ULTEM 1000 present high dielectric constant with the values of 3.1–3.5.[8] Low-k materials for PI-based dielectrics are still being pursued.

Generally, two strategies can be used for obtaining low-k PI-based polymers, according to the Clausius–Mossotti equation: (i) total number density of dipoles is reduced and (ii) dipole polarization intensity is lowered.[9–12]

$$\frac{k-1}{k+2}=\frac{4\pi}{3}N\alpha \tag{1}$$

where k is the dielectric constant of the material (in this work, PI), N represents the number of molecules per unit volume (density), α is the total polarization which contains the electronic (α_e), distortion (α_d), and orientation (α_o) polarization. Thus, cutting dielectric constant of PI, one impactful approach is to endow porous structure for the purpose of lowering the variable of N, fully taking advantage of the lowest k value of air ($k_{air} = 1$).[13–15] In practical, owing to the high relative permittivity of water (78.36, 25°C),[16] moisture absorption of low-k materials should be minimized to prevent dielectric-property intrusion from water. That is to say, good hydrophobicity plays a significant role in maintaining steady long-term operation of low-k PI-based polymers. Eletrospinning is a facile method to build porous

---

[1] School of Materials Science and Engineering, Harbin University of Science and Technology, Harbin, China

[2] Center for Composite Materials and Structures, Harbin Institute of Technology (HIT), Harbin, China

Corresponding author:

Guifen Gong, School of Materials Science and Engineering, Harbin University of Science and Technology, Harbin 150080, China.
Email: ggf-hust@163.com

structure containing uniform air nanovoids, compared with traditional technologies such as chemical etching and thermal decomposition.[17] This method can avoid tedious procedures for thermally labile precursors[14,18] and use of strong acid like hydrofluoric acid (HF) for etching.[19,20] Furthermore, using this method, other nanofillers can be tunable introduced into the PI matrix. Previous studies have shown that roughening the micro surface[21] and forming close interfaces to restrict the electron mobility[22] are favorable to hydrophobic and dielectric properties.

In addition to the aforementioned properties, low-*k* PI-based dielectrics will also be required for next-generation wearable micro/nanoelectronics that function in harsh service environments. Therefore, ultraviolet (UV)-light shielding properties are essential for steady operation of the dielectric layer in outdoor conditions. However, literature studying low-*k* materials has given little attention on these tolerances.[23]

In this work, we report the fabrication of low-*k* PI/titanium dioxide (TiO_2) composite nanofibers (NFs) via electrospinning. PI/TiO_2 composite NFs also present excellent UV-light shielding property with positive effects of TiO_2 NPs. A suitable TiO_2 content is required for balancing the hydrophobicity, low-*k* demands, and UV-light shielding properties of PI/TiO_2 composite NFs. Mechanical and thermal properties of PI/TiO_2 composite NFs are also studied. Such PI/TiO_2 composite NFs exhibit excellent dielectric properties (*k*: 2.17–2.32) and outstanding UV-light shielding properties, which can meet harsh working conditions.

Experiment

Materials

Analytical grade benzophenone-3,3′,4,4′-tetracarboxylic dianhydride (BTDA), *N*,*N*-dimethylacetamide (DMAc) and 4,4′-diaminodiphenyl ether (ODA, >99%) were purchased from Sigma-Aldrich, Shanghai, China. TiO_2 nanoparticles (NPs) were purchased from Aladdin Co. (average grain size: $\sim$25 nm). All reagents were used without any further purification. Pure PI NFs and PI/TiO_2 NFs were fabricated through thermal imidization of polyamic acid (PAA) and PAA/TiO_2 precursors. For pure PI NFs, the PAA precursor was solgel prepared by mixing (at 5°C for 12 h under nitrogen (N_2) atmosphere) BTDA and ODA (weight ratio of 1:1) into the DMAc solution. The PAA NFs were then subjected to an electrospinning process conducted at 10 kV and a constant feed rate of 0.3 mL h^{-1}. The thickness of the PAA NFs was optimized by controlling the electrospinning time for 5 h. As-obtained PAA NFs were further thermal imidized under step heat treatments at 80°C, 120°C, 200°C, and 250°C for 1 h each. The heating rate was 5°C min^{-1}. For fabricating PI/TiO_2 NFs, the PAA precursor was prepared using the same procedure, except that different weight percentages of TiO_2 NPs (2 wt%, 4 wt%, 6 wt%, and 8 wt%) were added to the PI matrix. The corresponding samples were designated as PI/TiO_2-2% NFs, PI/TiO_2-4% NFs, PI/TiO_2-6% NFs, and PI/TiO_2-8% NFs, depending on the TiO_2 content.

Characterization of PI/TiO_2 NFs

Samples structures and surface morphologies were determined via Fourier transform infrared (FTIR, AVATAR370, Thermo Nicolet, USA) with the range of 4000–400 cm^{-1} and a scanning electron microscopy (SEM, SIRION 200, FEI, USA) with energy-dispersive X-ray spectroscopy (EDS) mapping at an operation voltage of 20 kV. Thermal stability of samples was measured by a thermogravimetric analyzer (TGA, Pyris6, Prink-Elmer, USA), where the samples were heated from 50°C to 800°C (heating rate: 5°C min^{-1}) under N_2 protection. Tensile properties of pure PI NFs and PI/TiO_2 NFs were tested by universal tensile testing machine (Z050, Zwick Roell, Germany). Each type of nanofiber (NF) was measured five times and the results were averaged, according to standard ASTM D882. Specimen dimension was sliced as the tested dimensions with $120 \times 10 \times 0.25$ mm^3. The wettabilities between the water droplets and the surface of PI/TiO_2 NFs were measured at room temperature using a contact angle meter (JC2000C, Shanghai, China) equipped with a high-speed camera. Dielectric properties of PI/TiO_2 NFs membranes were measured using a broadband dielectric/impedance spectrometer (Novocontrol ALPHa-ANB, Germany) in the frequency range of 10^2–10^7 Hz. A ZHDS400-type magnetron sputter employing Au sputtering target was used to prepare sandwich-structured (i.e. Au deposited layer |PI/TiO_2 NFs|Au deposited layer) samples for dielectric testing. The dielectric constant and dielectric loss were calculated using the following equation

$$\varepsilon' = \frac{Cd}{\varepsilon_0 A} \tag{2}$$

where C represents the capacitance of PI/TiO_2 NFs, A is the deposited area, and ε' and ε_0 represent the dielectric constant of samples and a constant value in vacuum (8.85×10^{-12} F m^{-1}), respectively. UV-light shielding properties were tested twice with a Solar-500 xenon lamp (NBET Company, Beijing, China.) for stimulation of solar UV irradiation and a Cary 50 UV spectrophotometer, Salt Lake City, USA for UV-visible absorption with measured wavelength range of 200–-800 nm. The spectrophotometer was also used to measure the average UV-light absorption over wavelengths ranging from 200 nm to 400 nm. Samples were subjected to 90 h of solar irradiation (1000 W m^{-2}).

Results and discussion

Figure 1 illustrates the preparation of both pure PI NFs and PI/TiO_2 NFs. In the first step of PI/TiO_2 NF preparation, for

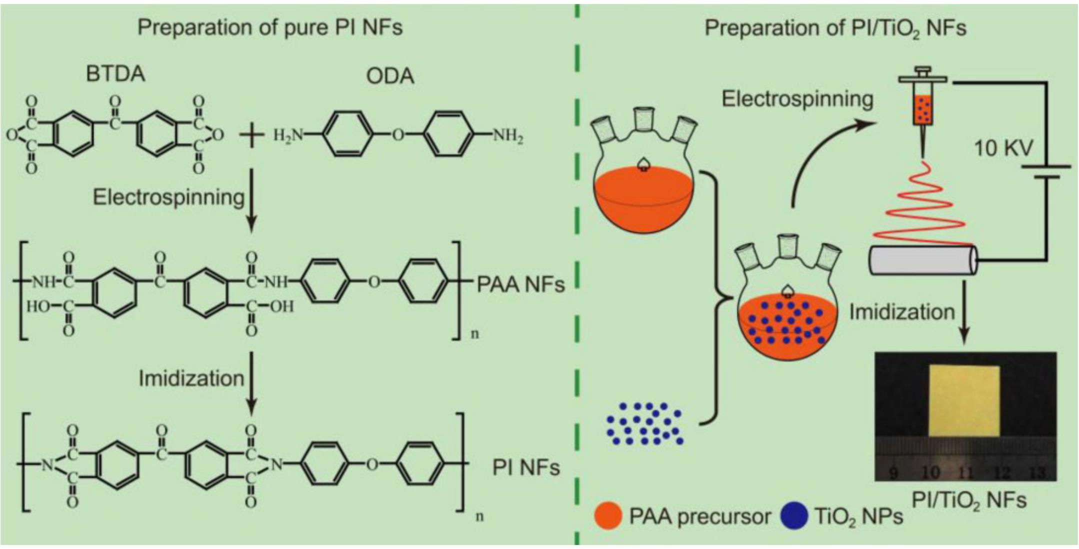

Figure 1. Flow-process diagram for preparation of pure PI NFs and PI/TiO_2 NFs. PI: polyimide; NF: nanofiber; TiO_2: titanium dioxide.

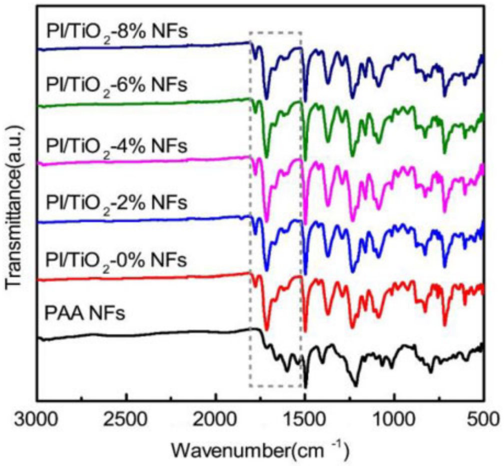

Figure 2. FTIR spectra of PAA NFs, pure PI NFs and PI/TiO_2 NFs. FTIR: Fourier transform infrared; PAA: polyamic acid; NF: nanofiber; PI: polyimide; TiO_2: titanium dioxide.

example, BTDA and ODA are firstly chosen as dianhydride and diamine monomers for the first step of preparation PAA precursor via solgel process. Various weight percentages (0–8 wt%) of TiO_2 NPs arethen separately added to the PAA solution. Subsequently, several PI/TiO_2 NF samples are obtained through electrospinning and imidization of the PAA/TiO_2 precursors.

The featured absorption peaks of PI are presented in the FTIR spectra of the pure PI NFs and the PI/TiO_2 NFs, as displayed in Figure 2. The peaks of 1780 cm^{-1}, 1720 cm^{-1} belong to C=O asymmetric and symmetric stretching in imide rings.[24–26] Other characteristic PI peaks, that is, at 1500 cm^{-1}, 1360 cm^{-1}, and 720 cm^{-1}, arise from benzene ring vibration, C–N stretching, and C=O bending,[27] respectively. Amide-based symmetric and asymmetric stretching vibration peaks (1650 cm^{-1} and 1547 cm^{-1}) are found in PAA NFs while they disappear in pure PI NFs and PI/TiO_2 NFs. The C=O stretching vibration peak (1715 cm^{-1}) of PAA NFs also transfers the C=O asymmetric (1780 cm^{-1}) and symmetric (1720 cm^{-1}) stretching in imide rings which is observed in pure PI NFs and PI/TiO_2 NFs. These results show PAA NFs have completed thermal imidization for preparation PI NFs. Different fingerprint regions between pure PI NFs and PI/TiO_2 NFs are focused on the low degree of wave number. The 600 cm^{-1} peak is found in PI/TiO_2 NFs, as belonged to Ti-O group vibration,[28,29] whereas the peak is absent from pure PI NFs.

The FTIR results show that we have successfully synthesized pure PI NFs and PI/TiO_2 NFs.

Figure 3 presents micro-morphologies of pure PI NFs and PI/TiO_2 NFs with low-magnification and high-magnification scales. All the PI/TiO_2 NFs samples retain fiber-like nanostructure without any collapse. The dispersion of titanium dioxide in PI/TiO_2 NFs is characterized by Figure 4. Adjacent pure PI NFs lap closely without any rough surface (see Figure 3(a) and (b)). Figure 3(c) to (j) and Figure 4 display that some TiO_2 NPs stick the rims of PI NFs and more TiO_2 NPs are coated in PI NFs to form a homogeneous dispersion system. These effectively prove successful combination of TiO_2 NPs and PI NFs for PI/TiO_2 NFs. Average diameters of all samples are nanosized in Figure 5, being consistent with logarithmic normal distribution. Pure PI NFs show the maximum average diameter among all samples, which is 250 nm (see Figure 5(a)). The average diameters of PI/TiO_2-2% NFs, PI/TiO_2-4% NFs, PI/TiO_2-6% NFs, and PI/TiO_2-8% NFs are 234 nm, 196 nm, 168 nm, and 220 nm, respectively (Figure 5(b) to (e)). Average diameters of PI/TiO_2 NFs become thinner with increasing content of TiO_2 NPs, expect for the ones of PI/TiO_2-8% NFs. Hence, it gets the optimization for obtaining the minimum average diameters with constantly adding

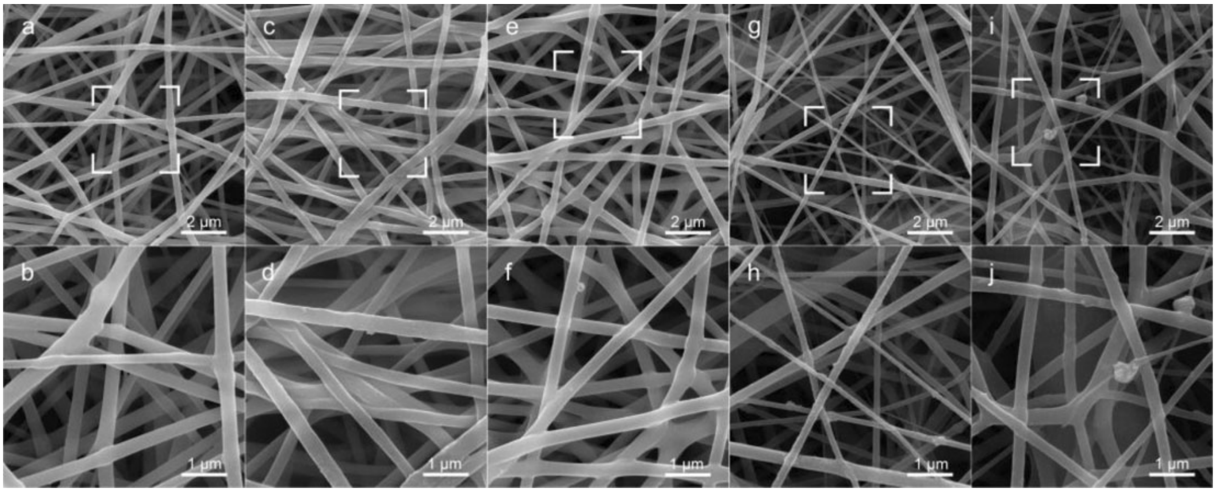

Figure 3. Low-magnification and high-magnification SEM images of pure PI NFs and PI/TiO_2 NFs. Pure PI (a and b); PI/TiO_2-2% NFs (c and d); PI/TiO_2-4% NFs (e and f); PI/TiO_2-6% NFs (g and h); PI/TiO_2-8% NFs (i and j). SEM: scanning electron microscopy; PI: polyimide; NF: nanofiber; TiO_2: titanium dioxide.

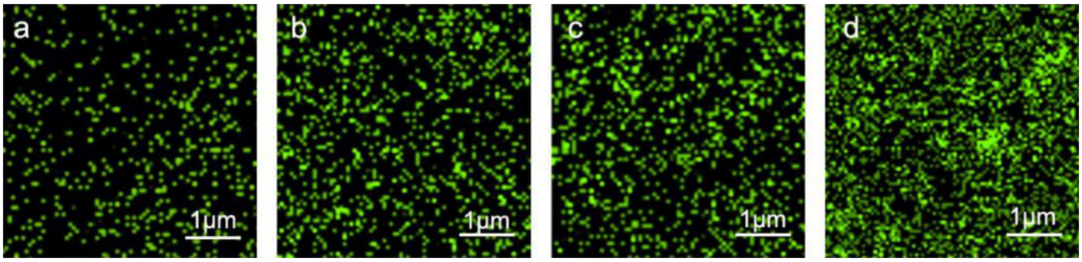

Figure 4. EDS element mapping of Ti from PI/TiO_2 NFs. (a) PI/TiO_2-2% NFs; (b) PI/TiO_2-4% NFs; (c) PI/TiO_2-6% NFs; (d) PI/TiO_2-8% NFs. EDS: energy-dispersive X-ray spectroscopy; NF: nanofiber; PI: polyimide; TiO_2: titanium dioxide.

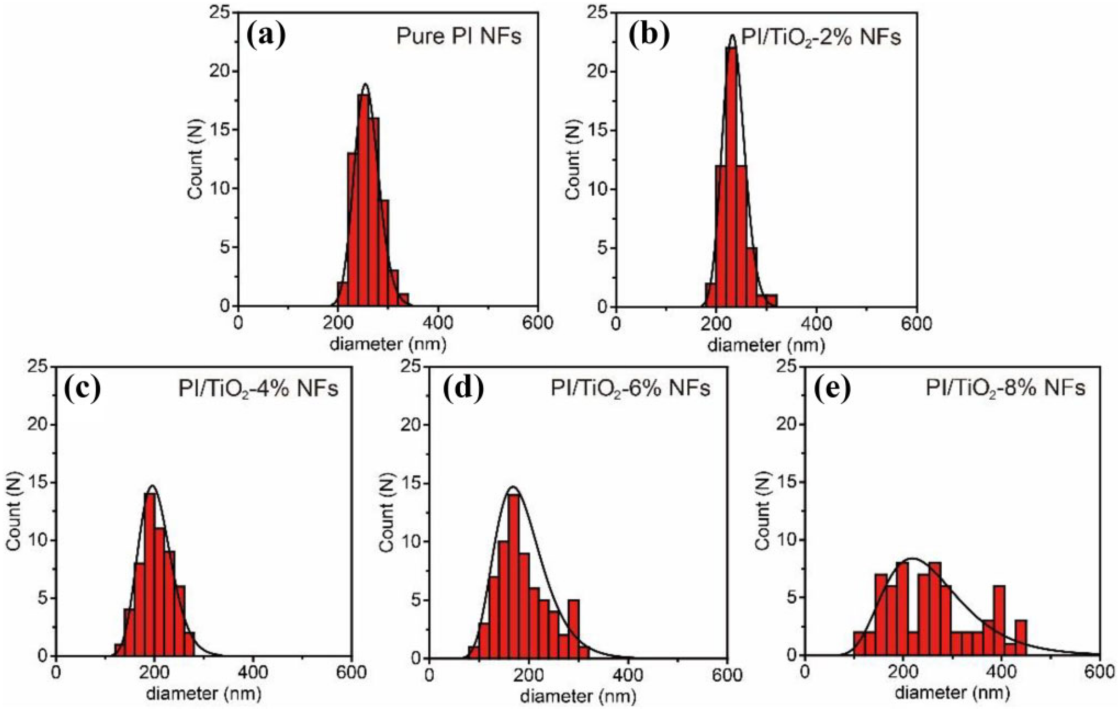

Figure 5. Histograms of diameter distribution for the (a) pure PI NFs, (b) PI/TiO_2-2% NFs, (c) PI/TiO_2-4% NFs, (d) PI/TiO_2-6% NFs, and (e) PI/TiO_2-8% NFs. PI: polyimide; NF: nanofiber; TiO_2: titanium dioxide.

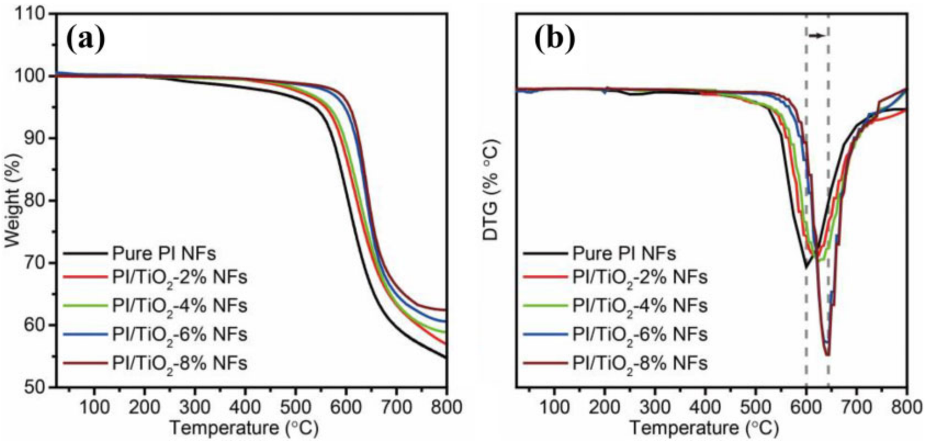

Figure 6. TG profiles (a) and derivative thermogravimetric analysis (DTG) curves (b) of pure PI NFs and PI/TiO_2 NFs. TG: thermogravimetric; PI: polyimide; NF: nanofiber; TiO_2: titanium dioxide.

TiO_2 in such PI/TiO_2 NFs (here is 6 wt% for TiO_2 in PI/TiO_2 NFs). A TiO_2 weight percentage exceeding 8 wt% results in increased viscosity of the precursor and, in turn, an uncontrollable electrospinning process occurring. This makes TiO_2 NPs agglomeration in the PI matrix (see Figure 3(i) and (j) and Figure 4). It finally leads to instability of average diameter with larger distribution in PI/TiO_2-8% NFs.

Thermal stability analyses (i.e. TG/DTG curves) of the PI/TiO_2 NFs are displayed in Figure 6. All PI/TiO_2 NFs samples show good high-temperature performances. Main thermal decomposition of pure PI NFs starts at 526°C and it achieves the maximum rate at 600°C (see Figure 6(b)). With the addition of TiO_2 NPs, both the temperatures of main thermal decomposition and ones of maximum rate shifts to higher temperature region. It implies that TiO_2 NPs can retard thermal decomposition in PI/TiO_2 NFs. The temperatures of the maximum rates are 621°C, 627°C, 640°C, and 646°C for PI/TiO_2-2% NFs, PI/TiO_2-4% NFs, PI/TiO_2-6% NFs, and PI/TiO_2-8% NFs, respectively. Furthermore, the quantification of thermal stability property is also applied with a heat resistance index as depicted below[30–36]

$$T_{\mathrm{h}} = 0.49 \times [T_5 + 0.6 \times (T_{30} - T_5)] \qquad (3)$$

where T_{h} represents the heat resistance index, T_5 and T_{30} are marked at the decomposing temperature at 5% and 30% weight loss from the results of TG curves, respectively. The related heat resistance index is 291.94°C for pure PI, 302°C for PI/TiO_2-2% NFs, 305°C for PI/TiO_2-4%, 313°C for PI/TiO_2-6%, and 317°C for PI/TiO_2-8% NFs (see Table 1). The addition of TiO_2 NPs can enhance the heat capacity of whole PI/TiO_2 NFs. Thus, it needs higher temperature for break the main chain of PI in the PI/TiO_2 NFs. SEM images also show TiO_2 NPs attach on PI NFs closely, which also helps PI/TiO_2 NFs obtain good antithermal decomposition ability, compared with the pure PI NFs. This result is ascribed to the contributions of compact interfaces between inorganic TiO_2 NPs and PI-based matrix for better thermal stability.

Table 1. Heat resistance index of all samples.

Samples	T_5 (°C)	T_{30} (°C)	$T_{\text{heat resistance index}}$ (°C)
Pure PI NFs	537	634	291
PI/TiO_2-2% NFs	559	655	302
PI/TiO_2-4% NFs	567	660	305
PI/TiO_2-6% NFs	596	668	313
PI/TiO_2-8% NFs	607	674	317

PI: polyimide; NF: nanofiber; TiO2: titanium dioxide.

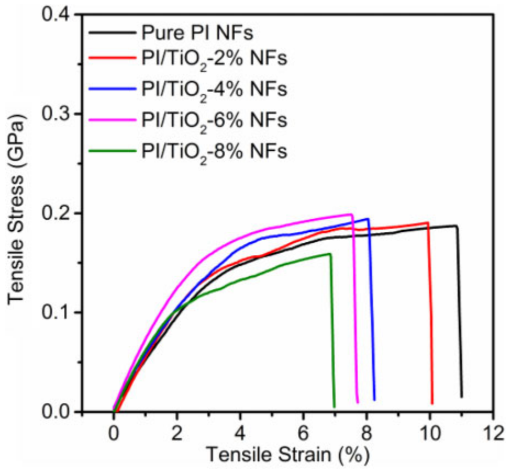

Figure 7. Strain–stress curves of pure PI NFs and PI/TiO_2 NFs. NF: nanofiber; PI: polyimide; TiO_2: titanium dioxide.

Figure 7 shows the correlation of tensile strain and stress in the pure PI and PI/TiO_2 NFs. Clearly, all samples contain two stages of elastic and plastic deformations before fracture. Tensile strain was 11% and tensile strength was 187 MPa for pure PI NFs. Both tensile strength and stress

Table 2. Tensile properties of pure PI NFs and PI/TiO_2 NFs.

Samples	Tensile stress (MPa)	Tensile strain (%)	Young's modulus (GPa)
Pure PI NFs	187	11	5.1
PI/TiO_2-2% NFs	190	10	5.5
PI/TiO_2-4% NFs	194	8	5.9
PI/TiO_2-6% NFs	198	8	7.3
PI/TiO_2-8% NFs	159	7	4.5

PI: polyimide; NF: nanofiber; TiO_2: titanium dioxide.

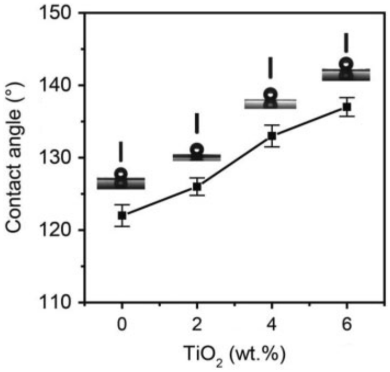

Figure 8. Static contact angle of pure PI NFs, PI/TiO_2-2% NFs, PI/TiO_2-4% NFs, and PI/TiO_2-6% NFs. PI: polyimide; NF: nanofiber; TiO_2: titanium dioxide.

Table 3. Comparison of CA in low-*k* PI-based dielectrics.

Samples	CA (°)	Reference
FG/PI films	74	Zhang et al.[27]
PI/GNR films	79	Liu et al.[38]
PI/APSZN films	84	Li et al.[39]
PI/Crown ether films	92	Li et al.[40]
homo-BPDA/BOA PI fiber	115	Yin et al.[41]
6FDA-based PI mats	125	Chen et al.[8]
PI/TiO_2-6% NFs	137	This work

CA: contact angle; PI: polyimide; FG: fluorographene; GNR: graphene nanoribbon; APSZN: amine-functionalized pure silica zeolite nanoparticles; BPDA: 3,3',4,4'-biphenyltetracarboxylic Dianhydride; BOA: 5-amino-2-(4-aminobenzene)benzoxazole; 6FDA: 4,4'-(hexafluoroisopropylidene)diphthalic anhydride; NF: nanofiber; TiO_2: titanium dioxide.

are positively correlated with increasing TiO_2 weight percentage in PI/TiO_2 NFs from Table 2, except for ones of PI/TiO_2-8% NFs. In fact, PI/ TiO_2-8% NFs show the minimum tensile strength of 159 MPa in the series of PI/TiO_2 composites, even being lower than that of pure PI. It might be attributed to weaker interfacial adherence[37] between over-agglomerated TiO_2 NPs and PI matrix to form rough surface of PI/TiO_2-8% NFs with a broadened average diameter distribution, being consistent with the results from Figure 3(i) and (j), Figures 4 and 5. Because PI/TiO_2-8% NFs show poorest mechanical properties, they are ruled out of the subsequent hydrophobic, dielectric, and UV-light shielding measurements. In contrast, PI/TiO_2-6% NFs are characterized by an extremely narrow diameter distribution and the smallest average diameter of all the composites. Therefore, the maximum tensile strength and Young's modulus are obtained for the PI/TiO_2-6% NFs, indicating that an optimized weight percentage of TiO_2 has a significant effect on the tensile properties of the PI/TiO_2 NFs.

To ensure regular functionality of Ultralarge-Scale Integrated Circuits (USICs) under humid environments, hydrophobicity is curial for dielectric constant composites. Figure 8 depicts the static contact angle of water in PI/TiO_2 NFs. Pure PI NFs have already retained good hydrophobicity with the static contact angle of 122°. Hydrophobic abilities of PI/TiO_2 NFs constantly increase with the addition of more TiO_2 NPs. The average static contact angles of water are 126°, 133°, and 137° for PI/TiO_2-2% NFs, PI/TiO_2-4% NFs, and PI/TiO_2-6% NFs, respectively. The hydrophobicity for the as-prepared PI/TiO_2 NFs is comparable to those reported in other studies (see Table 3).[8,27,38–41]

Figure 9(a) displays variations on dielectric loss of pure PI NFs and PI/TiO_2 NFs in the measured frequency from 10^2 to 10^7 Hz under room temperature. The dielectric constant of pure PI NFs is the lowest among the four samples, which is from 1.95 to 1.91 in the whole frequency. The ones of PI/TiO_2-2% NFs, PI/TiO_2-4% NFs, and PI/TiO_2-6% NFs are 2.17–2.04, 2.33–2.14, and 2.47–2.32, respectively. Based on the Clausius–Mossotti–Debye equation,

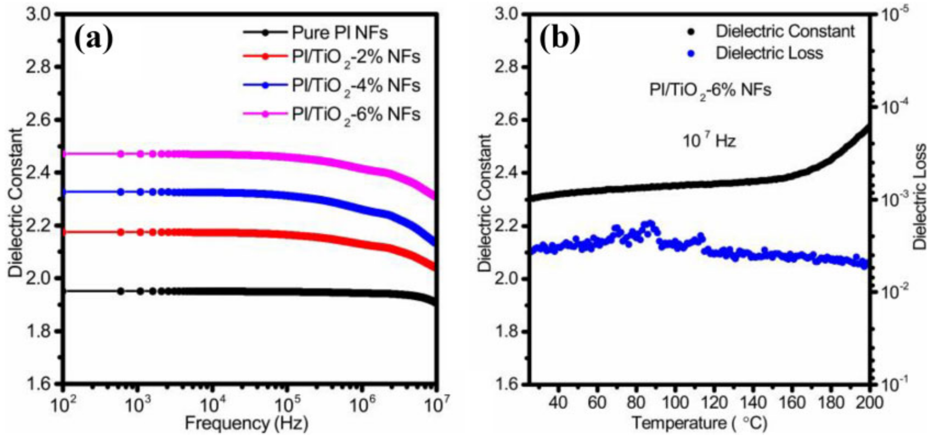

Figure 9. (a) Dielectric constant of pure PI NFs and PI/TiO_2 NFs in a continuous frequency range of 10^2–10^7 Hz and (b) temperature dependence of dielectric constant for PI/TiO_2-6% NFs at 10^7 Hz. PI: polyimide; NF: nanofiber; TiO_2: titanium dioxide.

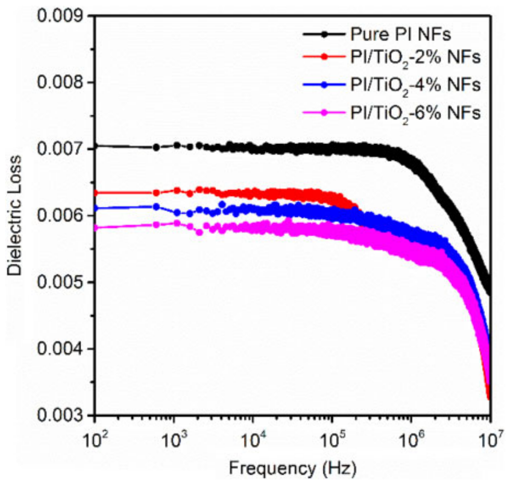

Figure 10. Dielectric loss of pure PI NFs and PI/TiO$_2$ NFs from 10^2 Hz to 10^7 Hz under room temperature. PI: polyimide; NF: nanofiber; TiO$_2$: titanium dioxide.

adding TiO$_2$ NPs inevitably increases dipole polarization, because of the higher intrinsic dielectric constant of TiO$_2$. Thanks to tightly integrated interface between TiO$_2$ NPs and PI matrix and porous structures with electrospinning technology, all PI/TiO$_2$ NFs still maintain relatively lower dielectric constant. Such PI/TiO$_2$ NFs also present very low dielectric loss, which are all lower than 0.0071 (see Figure 10). Figure 9(b) displays the temperature-dependent dielectric constant/loss in PI/TiO$_2$-6% NFs from 25°C to 200°C. Dielectric constant of PI/TiO$_2$-6% NFs is from 0.005. This proves relative stability of PI/TiO$_2$-6% NFs in both dielectric constant and dielectric loss in changeable operating-temperature usages.

We further investigate the UV-visible light absorption of PI/TiO$_2$ NFs with/without simulated solar irradiation to choose the wavelength range of 200–400 nm, as the selected UV-light, to study average UV-light absorption decay after a 90-h irradiation. Figure 11(a) and (b) shows

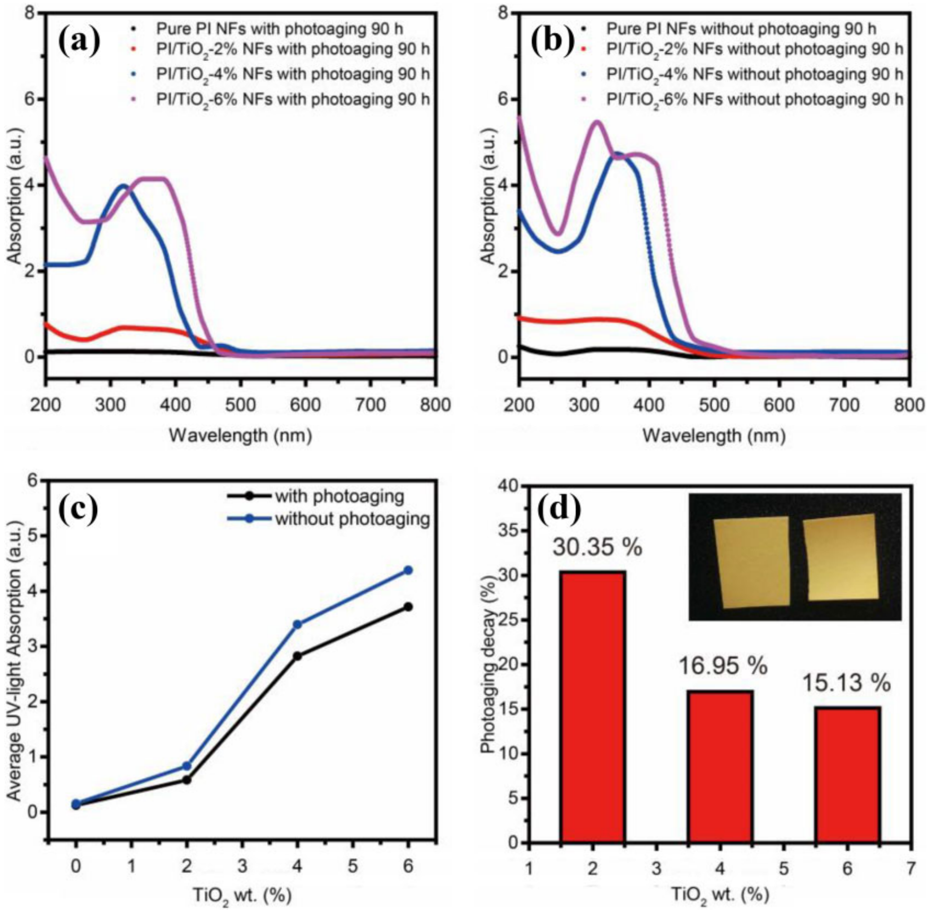

Figure 11. UV-vis absorption spectra of PI/TiO$_2$ NFs with solar irradiation (a) and without solar irradiation (b). (c) Average UV-light (200–400 nm) absorption of PI/TiO$_2$ NFs with/without solar irradiation. (d) Average UV-light absorption decay in PI/TiO$_2$ NFs. Inset is optical image on two pieces of PI/TiO$_2$-6% NFs without photoaging (left) and with photoaging (right). UV-vis: ultraviolet-visible; PI: polyimide; NF: nanofiber; TiO$_2$: titanium dioxide.

the UV-visible light absorption changes in pure PI and PI/TiO_2 NFs with/without solar irradiation. Pure PI NFs present a poor degree of UV-visible light absorbability, which is around 0.2. Meantime, PI/TiO_2 NFs samples present obviously reinforced UV-visible light absorbability, whose intensities are positive correlation to the weight percentage of TiO_2 NPs. Especially, we focus on UV-light absorbability to satisfy common UV-light protection demands. With increasing TiO_2 NPs content, average UV-light absorptions of PI/TiO_2 NFs are lifted from 0.16 to 4.38 under no solar irradiation condition and the ones increases from 0.12 to 3.71 after solar irradiation, showing the optimum anti UV-light irradiation in PI/TiO_2-6% NFs (Figure 11(c)). This is because TiO_2 has been wildly treated as a common light-screening agent and adding more TiO_2 NPs can continuously enhance PI/TiO_2 NFs absorption and scattering ability of UV-light to give good UV-light shielding. However, PI/TiO_2 NFs still suffer varying degrees of UV-light damage under a longtime irradiation (1000 W m^{-2} for 90 h) due to anisotropic photochemical reaction in the PI-based matrix[42] and existing defects between PI and TiO_2 NPs. Figure 11(d) shows the detailed average UV-light absorption decay in PI/TiO_2 NFs, which is 30.35% for PI/TiO_2-2% NFs, 16.95% for PI/TiO_2-4% NFs, and 15.13% for PI/TiO_2-6% NFs, respectively. Although the brims of PI/TiO_2-6% NFs is sort of warped after a 90-h solar irradiation, the color changes between the two pieces of PI/TiO_2-6% NFs with/without solar photoaging (Figure 11(d), inset) can be negligible.

Conclusions

In summary, pure PI NFs and PI/TiO_2 NFs are successfully fabricated with the average diameters of 200–250 nm via electrospinning. Adding TiO_2 is an efficient route to improve thermal stability properties of PI/TiO_2 NFs, evidenced by the high heat resistance index (317°C) in the PI/TiO_2-8% NFs. However, due to the excess TiO_2 NPs agglomeration and larger turbulence of average diameters, PI/TiO_2-8% NFs exhibit the poorest mechanical tensile properties. In comparison, PI/TiO_2-6% NFs obtained the best tensile properties among all samples, which are 198 MPa for tensile stress, 7% for tensile strain, and 7.3 GPa for Young's modulus, separately. PI/TiO_2-6% NFs are also evidenced owning excellent hydrophobicity and UV-light shielding properties after being checked with static contact angle measurement and a 90-h solar irradiation. Based on the contact angle ($\sim 137°$) and average anti UV-light absorption decay (15.13%) realized, the PI/TiO_2-6% NFs are considered the optimum PI/TiO_2 NF sample. Further investigation of the dielectric properties reveals that, owing to porous structures and compact TiO_2 NP/PI NFs interfaces, relatively low dielectric constants (k: 2.17–2.32) and low dielectric losses (<0.0071) are achieved. The PI/TiO_2 NFs can serve as an excellent alternative to replace current low constant materials for higher hydrophobicity and anti UV-light photoaging demands in microelectronics.

Author contribution

Guifen Gong contributed equally to this work.

Declaration of conflicting interests

The author(s) declared no potential conflicts of interest with respect to the research, authorship, and/or publication of this article.

Funding

The author(s) disclosed receipt of the following financial support for the research, authorship, and/or publication of this article: This work was financially supported by the National Natural Science Foundation of China (grant no. 5160030627).

ORCID iD

Lei Wang https://orcid.org/0000-0002-2199-795X

References

1. Zhao CJ, Wei XN, Huang YW, et al. Preparation and unique dielectric properties of nanoporous materials with well-controlled closed-nanopores. *Phys Chem Chem Phys* 2016; **28**: 19183–19193.
2. Jiang T, Zhu B, Ding SJ, et al. High-performance ultralow dielectric constant carbon-bridged mesoporous organosilica films for advanced interconnects. *J Mater Chem C* 2014; **32**: 6502–6510.
3. Grill A, Gates SM, Ryan TE, et al. Progress in the development and understanding of advanced low k and ultralow k dielectrics for very large-scale integrated interconnects-state of the art. *Appl Phys Rev* 2014; **1**: 011306.
4. Valeevg AS and Krasnikov Y. Manufacturing technology of intra- and interchip interconnects for modern ULSIs: review and concepts of development. *J Mater Sci Mater El* 2015; **44**: 154–172.
5. Liu ZH, Pang L, Li Q, et al. Hydrophilic porous polyimide/β-cyclodextrin composite membranes with enhanced gas separation performance and low dielectric constant. *High Perform Polym* 2017; **30**: 446–455.
6. Kıvılcım N, Seckin T and Koytepe S. Porous pyridine based polyimide–silica nanocomposites with low dielectric constant. *J Porous Mater* 2013; **20**: 709–718.
7. Song GL, Wang LN, Liu DD, et al. Gas transport properties of polyimide membranes bearing phenyl pendant group. *High Perform Polym* 2017; **30**: 161–171.
8. Chen F, Bera D, Banerjee S, et al. Low dielectric constant polyimide nanomats by electrospinning. *Polym Adv Technol* 2012; **23**: 951–957.
9. Baklanov MR and Maex K. Porous low dielectric constant materials for microelectronics. *P Phil Trans R Soc A* 2006; **364**: 201–215.

10. Kurinchyselvan S, Sasikumar R, Ariraman M, et al. Low dielectric behavior of amine functionalized MCM-41 reinforced polyimide nanocomposites. *High Perform Polym* 2015; **28**: 842–853.
11. Dong J, Yang CR, Cheng Y, et al. Facile method for fabricating low dielectric constant polyimide fibers with hyperbranched polysiloxane. *J Mater Chem C* 2017; **5**: 2818–2825.
12. Shamiryan D, Abell T, Iacopi F, et al. Low-k dielectric materials. *Mater Today* 2004; **7**: 34–39.
13. Zhang YH, Yu L, Zhao LH, et al. Dielectric and thermal properties of polyimide–poly(ethylene oxide) nanofoamed films. *J Electron Mater* 2012; **41**: 2281–2285.
14. Li Z, Zou H and Liu P. Morphology and properties of porous polyimide films prepared through thermally induced phase separation. *RSC Adv* 2015; **47**: 37837–37842.
15. Chen W, Liu FL, Ji M, et al. Synthesis and characterization of low-CTE polyimide films containing trifluoromethyl groups with water-repellant characteristics. *High Perform Polym* 2016; **29**: 501–512.
16. Haynes WM, Lide DR and Bruno TJ. *CRC Handbook of Chemistry and Physics*. Boca Raton, FL: CRC Press, 2017, p. 4.
17. Ruan KP, Guo YQ, Tang YS, et al. Improved thermal conductivities in polystyrene nanocomposites by incorporating thermal reduced graphene oxide via electrospinning-hot press technique. *Compos Commun* 2018; **10**: 68–72.
18. Ju J, Wang Q, Wang T, et al. Low dielectric, nanoporous fluorinated polyimide films prepared from PCL-PIPCL triblock copolymer using retro-Diels–Alder reaction. *J Colloid Interface Sci* 2013; **404**(suppl C): 36–41.
19. Lee J, Lee S, Kim K, et al. Low dielectric transparent poly(-amide-imide) thin film with nano scale porous structure. *Macromol Res* 2017; **25**: 1115–1120.
20. Zhang YH, Yu L, Su Q, et al. Fluorinated polyimide–silica films with low permittivity and low dielectric loss. *J Mater Sci* 2012; **47**: 1958–1963.
21. Gong G, Gao K, Wu J, et al. A highly durable silica/polyimide superhydrophobic nanocomposite film with excellent thermal stability and abrasion-resistant performance. *J Mater Chem A* 2015; **3**: 713–718.
22. Liu LP, Lv FZ, Li PG, et al. Preparation of ultra-low dielectric constant silica/polyimide nanofiber membranes by electrospinning. *Compos A Appl Sci* 2016; **84**: 292–298.
23. Tang YS, Dong WC, Tang L, et al. Fabrication and investigations on the polydopamine/KH-560 functionalized PBO fibers/cyanate ester wave-transparent composites. *Compos Commun* 2018; **8**: 36–41.
24. Wang Z, Zhang B, Yu H, et al. Microporous polyimide networks with large surface areas and their hydrogen storage properties. *Chem Commun* 2010; **46**: 7730–7732.
25. Park S, Kim K, Kim JC, et al. Synthesis and nonvolatile memory characteristics of thermally, dimensionally and chemically stable polyimides. *Polymer* 2011; **5**: 2170–2179.
26. Abe K, Nagao D and Konno M. Fabrication of highly refractive $BaTiO_3$ nanocomposite films using heat resistant polymer as matrix. *Eur Polym J* 2013; **49**: 3455–3459.
27. Zhang PP, Zhao JP, Zhang K, et al. Fluorographene/polyimide composite films: mechanical, electrical, hydrophobic, thermal and low dielectric properties. *Compos A Appl Sci* 2016; **84**: 428–434.
28. Zheng M, Gu M, Jin Y, et al. Preparation, structure and properties of TiO_2–PVP hybrid films. *Mater Sci Eng B* 2000; **77**: 55–59.
29. Zhou Y, Wang XY, Wang H, et al. Enhanced dye-sensitized solar cells performance using anatase TiO_2 mesocrystals with the Wulff construction of nearly 100% exposed 101 facets as effective light scattering layer. *Dalton Trans* 2014; **43**: 4711–4719.
30. Gu JW, Dong WC, Tang YS, et al. Ultralow dielectric, fluoride-containing cyanate ester resins with improved mechanical properties and high thermal and dimensional stabilities. *J Mater Chem C* 2017; **28**: 6929–6936.
31. Gu JW, Lv ZY, Wu YL, et al. Dielectric thermally conductive boron nitride/polyimide composites with outstanding thermal stabilities via in-situ polymerization-electrospinning-hot press method. *Compos A Appl Sci* 2017; **94**: 209–216.
32. Yang XT, Guo YQ, Luo X, et al. Self-healing, recoverable epoxy elastomers and their composites with desirable thermal conductivities by incorporating BN fillers via in-situ polymerization. *Compos Sci Technol* 2018; **164**: 59–64.
33. Yang XT, Tang L, Guo YQ, et al. Improvement of thermal conductivities for PPS dielectric nanocomposites via incorporating NH_2-POSS functionalized nBN fillers. *Compos A* 2017; **101**: 237–242.
34. Guo YQ, Xu GJ, Yang XT, et al. Significantly enhanced and precisely modeled thermal conductivity in polyimide nanocomposites with chemically modified graphene via in situ polymerization and electrospinning-hot press technology. *J Mater Chem C* 2018; **6**: 3004–3015.
35. Gu JW, Liang CB, Dang J, et al. Ideal dielectric thermally conductive bismaleimide nanocomposites filled with polyhedral oligomeric silsesquioxane functionalized nanosized boron nitride. *RSC Adv* 2016; **6**: 35809–35814.
36. Gu JW, Zhang QY, Dang J, et al. Preparation and properties of polystyrene/SiCw/SiCp thermal conductivity composites. *J Appl Polym Sci* 2012; **124**: 132–137.
37. Gibeop N, Lee DW, Prasad CV, et al. Effect of plasma treatment on mechanical properties of jute fiber/poly(lactic acid) biodegradable composites. *Adv Compos Mater* 2013; **22**: 389–399.
38. Liu XX, Li YP, Guo WM, et al. Dielectric and mechanical properties of polyimide composite films reinforced with grapheme nanoribbon. *Surf Coat Tech* 2017; **320**: 497–502.
39. Li Q, Liao GF, Zhang SL, et al. Effect of adjustable molecular chain structure and pure silica zeolite nanoparticles on thermal, mechanical, dielectric, UV shielding and hydrophobic

properties of fluorinated copolyimide composites. *Appl Surf Sci* 2018; **427**: 437–450.

40. Li Y, Zhao JQ, Yuan YC, et al. Polyimide/crown ether composite films with necklace-like supramolecular structure and improved mechanical, dielectric, and hydrophobic properties. *Macromolecules* 2015; **48**: 2173–2183.
41. Yin CQ, Dong J, Zhang DB, et al. Enhanced mechanical and hydrophobic properties of polyimide fibers containing benzimidazole and benzoxazole units. *Eur Polym J* 2015; **67**: 88–98.
42. Hasegawa M and Taira Y. Nematic homogeneous photo alignment by polyimide exposure to linearly polarized UV. *J Photopolym Sci Tech* 1995; **8**: 241–248.